EDGE ARTICLE

Check for updates

Tailoring dual-hydrophobic microenvironment for tandem CO$_2$/CO feedstock to enhance CO$_2$ electroreduction on Cu-based catalysts†

Tete Zhao,[a] Ziyao Zhou,[a] Xiao Wang,[a] Kuiming Liu,[a] Jialei Chen,[a] Kang Liu,[a] Yue Li,[a] Meng Yu, [ID] *[a] Yan Xu,*[b] Zhenhua Yan, [ID] [a] Lifang Jiao [ID] [a] and Fangyi Cheng [ID] *[a]

Achieving high selectivity for value-added products in the electrochemical reduction of CO$_2$ remains challenging due to severe hydrogen evolution, sluggish CO$_2$ mass transport and low *CO coverage. Herein, we integrate aerophilic SiO$_2$ and polymer-functionalized copper nanoparticles (Cu-poly) to construct a hierarchical-hydrophobic Cu-poly/SiO$_2$ composite, which limits the accessibility of H$_2$O, improves the local concentration of CO$_2$ and enhances the dimerization of *CO–*CO. Comprehensive investigation using X-ray absorption spectroscopy, *in situ* infrared spectroscopy and molecular dynamics simulations indicates that the polymer and SiO$_2$ elevate the oxidation state of Cu species, enhance the CO$_2$ diffusion coefficients (from 5.27×10^{-7} on Cu to 8.81×10^{-7} cm^2 s^{-1} on Cu-poly/SiO$_2$) and enrich the local *CO concentration. The Cu-poly/SiO$_2$ electrode delivers an enhanced faradaic efficiency of 60.54% for C$_{2+}$ products, compared to 46.1% of Cu at 600 mA cm^{-2}. Notably, a high FE of 36.91% and partial current density of 221.46 mA cm^{-2} are achieved for C$_2$H$_4$ generation in membrane electrode assembly devices adopting an aqueous bicarbonate electrolyte. This work provides a valuable insight into designing catalytic microenvironments of electrocatalysts for enhancing carbonaceous products by facilitating the co-electrolysis of CO$_2$ and *in situ*-generated *CO.

Introduction

Electrochemical CO$_2$ reduction reaction (CO$_2$RR) to value-added chemicals and fuels using renewable electricity on Cu-based electrocatalysts provides a promising strategy to achieve carbon neutrality.[1–5] However, severe flooding of the gas diffusion layer (GDL), poor *CO–*CO coupling and sluggish CO$_2$ mass transport impede the high-efficiency formation of multicarbon (C$_{2+}$) products.[6–9] An appealing method is to regulate the reaction microenvironment of catalysts, including the ratio of H$_2$O and CO$_2$, the local coverage of *CO, and the concentration of cations through molecular engineering, functionalized polymers, ionomers, and similar modifications. This limits H$_2$O accessibility, enhances CO$_2$ diffusion dynamics and stabilizes key intermediates, ultimately improving the formation rate of carbonaceous products.[10–17] Although these strategies accelerate the generation of value-added products in a three-electrode

system, they still confront obstacles when employed as a membrane electrode assembly (MEA) electrolyzer to achieve a commercial current density for CO$_2$RR. Moreover, the hydrophobicity of the catalytic layer (CL) and CO$_2$ mass transfer channel in GDL are susceptible to destruction due to the organically modified layers peeling off, caused by rapid evolution of product bubbles.

Furthermore, an alternative strategy to tailor the reaction microenvironments involves the direct incorporation of hydrophobic additives, such as polytetrafluoroethylene (PTFE), polyvinylidene fluoride (PVDF), pyridine-containing microgels, graphene, metal–organic frameworks (MOFs) and covalent organic frameworks (COFs), into the vicinity of electrocatalysts, which improves the mass transfer of CO$_2$, the local pH and coverage of CO, thus enhancing the efficiency of CO$_2$ electroreduction.[18–22] Although these additives could optimize the microenvironments of catalysts, the electrochemical-adsorption/desorption behavior of reactant and intermediates on these additional promoters is still poorly understood, leading to undesirable reaction pathways, decreasing the selectivity for C$_{2+}$ products. More importantly, the organic backbone of additives can become deactivated and gradually dissolve into the electrolyte under an electric field during prolonged electrolysis. This mainly occurs due to the polarity of H$_2$O through the anion exchange membrane (AEM) from the anolyte, reducing the organic fluorine content and thus

[a]State Key Laboratory of Advanced Power Sources, Key Laboratory of Advanced Energy Materials Chemistry (Ministry of Education), Engineering Research Center of High-Efficiency Energy Storage (Ministry of Education), Frontiers Science Center for New Organic Matter, College of Chemistry, Nankai University, Tianjin 300071, China. E-mail: nkyu2023@nankai.edu.cn; fycheng@nankai.edu.cn

[b]College of Energy Storage Technology, Shandong University of Science and Technology, Qingdao, Shandong 266590, China. E-mail: xuyan2020@sdust.edu.cn

† Electronic supplementary information (ESI) available. See DOI: https://doi.org/10.1039/d5sc01226k

increasing hydrophilicity.[23,24] Therefore, it is challenging to achieve the hydrophobic requirements of the CL of gas diffusion electrodes (GDEs) by relying solely on additives under industrial-grade current electrolysis.

Herein, we report the integration of inorganic SiO_2 with robust hydrophobicity into the CL of polymer-functionalized Cu nanoparticles (Cu-poly) towards efficient CO_2RR. Dual-hydrophobic catalytic characteristics are designed for Cu-poly/SiO_2 composites by considering both the surface and interface. This approach combines modification and additive engineering strategies to enhance CO_2 electroreduction. Our results demonstrate that the production rate of C_2H_4 is significantly improved on the dual-hydrophobic Cu-poly/SiO_2 electrodes compared to bare Cu, surface-modified Cu-poly and Cu/SiO_2 electrodes in MEA devices by suppressing the hydrogen evolution reaction (HER). Meanwhile, we investigate the effect of polymer and SiO_2 on the surface oxidation state of Cu and the composition of CO_2RR products. The positive effect of the local concentration of CO_2/H_2O and *in situ*-generated CO on the production of C_2H_4 is investigated by a comprehensive combination of spectroscopic analysis, electrochemical performance evaluation and molecular dynamics (MD) simulation results. The SiO_2 and polymer components are favorable for enriching and accelerating CO_2 mass transfer, limiting H_2O accessibility and elevating local CO concentration. This work elucidates the engineering of dual-hydrophobic microenvironments *via* integration of surface and interface modifications on electrocatalysts, providing further perspectives on the co-electrolysis mechanism of CO_2 and CO in modified-Cu electrodes towards C_2H_4.

Results and discussion

To design the dual-hydrophobic catalytic microenvironments, bare Cu nanoparticles were synthesized by a facile liquid-phase reduction method using sodium borohydride.[25] The fluorine-polymer-functionalized Cu (Cu-poly) was prepared by *in situ* radical polymerization under the initiation of azobisisobutyronitrile with precursor molecules of trifluoromethyl methacrylate and 3-(methacryloyloxy)propyltrimethoxysilane.[26] Afterwards, the obtained Cu-poly and hydrophobic SiO_2 were ultrasonically mixed to carefully fabricate the Cu-poly/SiO_2 composites. Fig. 1a and b comparatively illustrate the different catalytic microenvironments of bare Cu and Cu-poly/SiO_2 composites. For hydrophilic GDEs, the surface of Cu is prone to being wetted by an aqueous electrolyte, resulting in sluggish CO_2 mass transfer, excessive H_2O supply and low *CO coverage (Fig. 1a). It is reasonable that the HER would be more favourable on hydrophilic Cu than the CO_2RR.[20] In contrast, the GDEs covered by Cu-poly/SiO_2 consist of aerophilic SiO_2 and polymer-
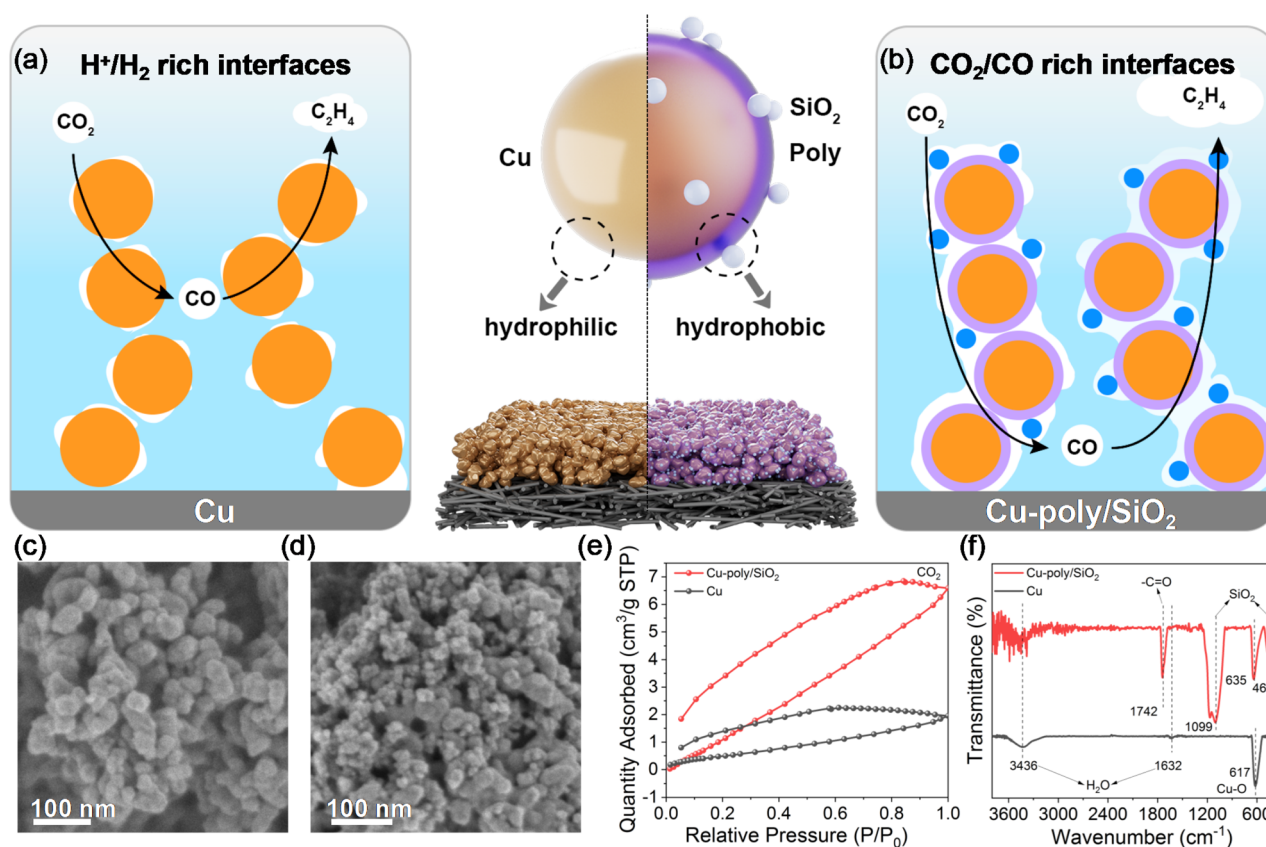

Fig. 1 Catalyst design, preparation and characterization. Schematic illustration of the hydrophilic microenvironments of (a) Cu and (b) the dual-hydrophobic microenvironment of Cu–poly/SiO_2. (c and d) SEM images of (c) Cu and (d) Cu–poly/SiO_2. (e) CO_2 adsorption/desorption isotherm curves of Cu and Cu–poly/SiO_2. (f) FTIR spectra of Cu and Cu–poly/SiO_2.

functionalized Cu, forming abundant gas–liquid–solid three-phase interfaces and benefiting the mass transfer of reactants (Fig. 1b). SiO_2 and polymer endow Cu-poly/SiO_2 with robust hydrophobicity from the interfaces and surface, respectively. These characteristics play multiple roles in facilitating the mass transfer of CO_2 and decreasing the local concentration of H_2O, due to the interconnected gas diffusion networks and strong hydrophobicity. More importantly, the dual-hydrophobicity reaction microenvironment originating from the polymer and SiO_2 could accelerate the *in situ* generation of CO during CO_2RR, owing to the absence of H_2O on the surface of Cu. Consequently, Cu-poly/SiO_2 promotes the local concentration of CO on Cu and then achieves the co-electrolysis of CO_2 generating CO, which would contribute to the highly efficient generation of C_{2+} products.[27]

As shown in scanning electron microscopy (SEM, Fig. 1c) and high-resolution transmission electron microscopy (HRTEM, Fig. S1a, ESI†) images, the prepared Cu presents an irregular spherical morphology, accompanied by the minor facets of (111) and (220) of Cu_2O and the major facets of (111), (200) and (220) of Cu.[28] The phase structure and corresponding facets are also revealed by the X-ray diffraction (XRD) patterns, HRTEM, and selected-area electron diffraction (SAED) images (Fig. S1b–f and S2, ESI†). Furthermore, high-angle annular dark-field STEM (HADDF-STEM, Fig. S3a–c, ESI†) images also reveal the irregular morphology and exposed facets. The corresponding elemental mapping images show that Cu and O are uniformly distributed (Fig. S3d–f, ESI†). To evaluate the stability of hydrophobicity for Cu and Cu-poly/SiO_2, we employed the ultrasonication method to compare their behaviours. The results show that the Cu powder quickly disperses in H_2O after 30 min, whereas due to the combined effect of the polymer and SiO_2, Cu-poly/SiO_2 remains floating on the surface of H_2O after 30 min, demonstrating stable hydrophobicity (Fig. S4, ESI†). Benefiting from the durable hydrophobic characteristics, Cu-poly/SiO_2 offers an abundant reaction vicinity to adsorb and activate CO_2 molecules. To reveal the synergistic effects of hydrophobic SiO_2 and polymer on CO_2 adsorption, we conducted the measurement of CO_2 adsorption–desorption isotherms under ice-water mixtures, and the results show that Cu-poly/SiO_2 possesses an enhanced adsorption capacity of CO_2 compared to Cu according to the normalized adsorption value (0.108 on Cu-poly/SiO_2 *vs.* 0.075 on Cu) by the surface area at the fixed pressure of $P/P_0 = 1$ (Fig. 1e and S5, ESI†).

FTIR spectra of Cu and Cu-poly/SiO_2 were recorded to further investigate the surface composition and bonding information. As depicted in Fig. 1f, the broad peaks corresponding to the stretching (3436 cm^{-1}) and bending vibrations (1632 cm^{-1}) of H_2O are clearly observed on bare Cu.[29] In comparison, these signals are not obvious on Cu-poly/SiO_2, which indicates that the polymer and SiO_2 could limit the adsorption of H_2O. Notably, there is a sharp peak located at 617 cm^{-1}, which could be attributed to the stretching vibration of the Cu–O bond in Cu_2O, which further confirms the oxidation of Cu.[30] However, the wavenumber of the Cu–O bond shifts from 617 to 635 cm^{-1} and the stretching vibration of Cu–O is stronger in Cu-poly/SiO_2 than that in Cu, implying that Cu-poly/SiO_2 is more readily

oxidized due to polymerization. This result is further supported by the vibration of the Cu–O bond in the Raman spectra of Cu and Cu-poly/SiO_2 (Fig. S6, ESI†). Furthermore, the vibrations located at 467 and 1099 cm^{-1} are attributed to the Si–O bonds, confirming the incorporation of SiO_2 into Cu-poly/SiO_2.[31] More importantly, the peak located at 1742 cm^{-1} is attributed to the vibrations of –C=O in the polymer that coats the surface of Cu.[32]

To examine the microstructure, aberration-corrected high-angle annular dark-field scanning transmission electron microscopy (AC-HAADF-STEM) images were collected on Cu-poly/SiO_2. The resulting images reveal that the catalysts exhibit a polycrystalline structure containing both Cu and Cu_2O phases (Fig. S2, ESI†), along with abundant pores generated by the aggregation of Cu-poly and SiO_2. These pores facilitate the efficient transport of CO_2 while limiting the accessibility of H_2O (Fig. 2a and S7a, b, ESI†). Furthermore, the high-resolution AC-HAADF-STEM image clearly identifies well-defined interfaces between Cu_2O, the polymer and SiO_2. Notably, the oxidized Cu particles are tightly encapsulated by the polymer with the interface, indicating that the polymer-coated Cu interacts with SiO_2 (Fig. 2b). In addition, the corresponding annular bright field (ABF)-STEM images further confirm these observations, suggesting that this structure may inhibit hydrogen production while activating inert CO_2 molecules.[33] The observed lattice fringes exhibit an interplanar spacing of 0.24 nm, which is ascribed to the (111) facet of Cu_2O (Fig. 2c and S7c, d, ESI†).[34] Energy dispersive spectrometer (EDS) mapping analysis reveals a homogeneous distribution of Cu, Si, F, C, and O across Cu-poly/SiO_2 (Fig. 2d–i and S8, ESI†).

Additionally, we also measured the solid nuclear magnetic resonance (NMR) spectrum of ^{13}C, ^{19}F and ^{1}H to analyze the surface elemental composition after polymerization in Cu-poly. The ^{13}C spectra show five sharp peaks located at chemical shifts of 176.7, 125.5, 61.5, 45.8, and 18.5 ppm, corresponding to the functional groups of –O–C=O, –C≡N, –O–C, and the carbon in the main chains of polymer (–CH_2/–CH/–C) and –CH_3, respectively (Fig. 3a). Furthermore, the ^{19}F and ^{1}H spectra were also recorded on Cu-poly (Fig. S9, ESI†). These NMR results indicate that the polymer successfully coated the surface of Cu, a conclusion also corroborated by HADDF-STEM images and Fourier-transform infrared (FTIR) spectra, as shown in Fig. 1f and 2a–d. In addition, the XPS surveys of Si and F spectra also indicate that the polymer is coated on the surface of Cu (Fig. S10a–c, ESI†).

Previous studies have highlighted the key role of the surface oxidation state of Cu in regulating selectivity towards C_{2+} products.[35] To investigate the effect of SiO_2 and polymer on this feature, we comparatively analyzed the chemical valence of Cu species in Cu, Cu-poly and Cu-poly/SiO_2 using X-ray photoelectron spectroscopy (XPS) and X-ray absorption spectroscopy (XAS). Auger LMM spectra of Cu exhibit an obvious shift in binding energy from 569.9 eV of bare Cu to 570.2 eV of Cu-poly/SiO_2, indicating a higher oxidation state of Cu in Cu-poly/SiO_2 (Fig. 3b and S10d, ESI†). The X-ray absorption near-edge structure (XANES) spectra of Cu K-edge demonstrate that the absorption edge positions of Cu, Cu-poly, Cu-poly/SiO_2 and all
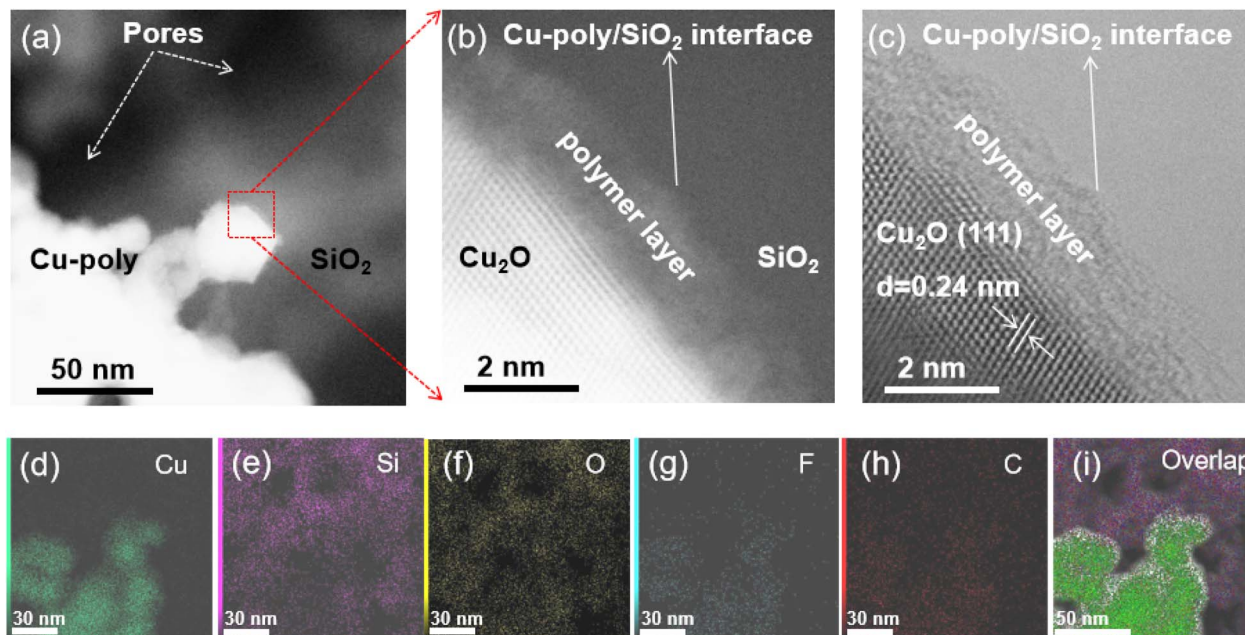
Fig. 2 Structural characterization of Cu-poly/SiO₂. (a and b) HAADF-STEM images. (c) Annular bright field (ABF)-STEM image. (d–i) Elemental mapping images of Cu-poly/SiO₂. Colors in (d–i): Cu green, O yellow, Si pink, C red, F cyan.
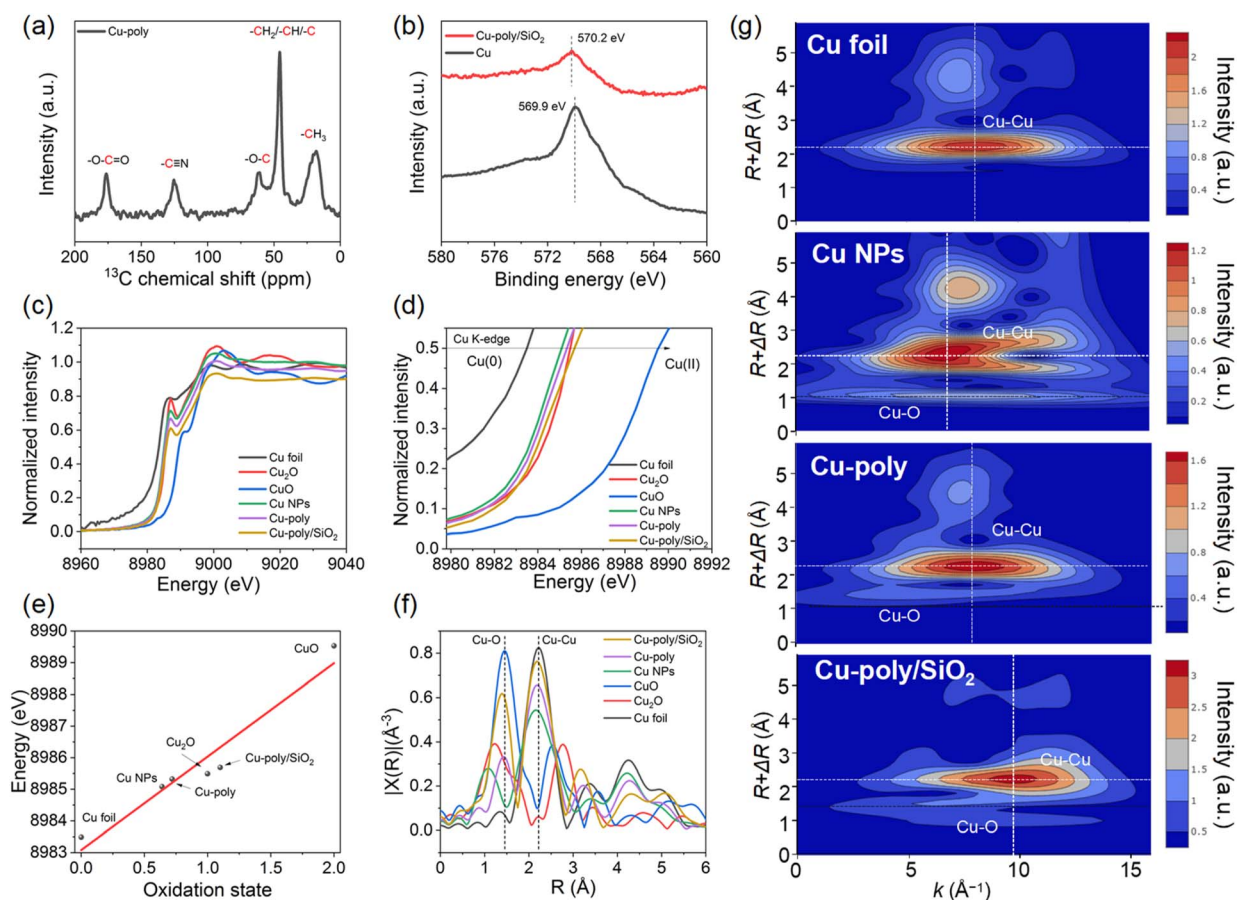

Fig. 3 Surface oxidation and chemical valence of Cu. (a) Solid NMR spectrum of ^{13}C. (b) Cu Auger LMM spectra of Cu and Cu-poly/SiO₂. (c and d) Normalized Cu K-edge XANES spectra of Cu, Cu-poly, Cu-poly/SiO₂ and Cu-foil, Cu₂O, CuO standard. (e) Average oxidation state of Cu in Cu, Cu-poly and Cu-poly/SiO₂ based on Cu foil, Cu₂O and CuO references. (f) Cu K-edge Fourier transform (FT) EXAFS spectra of Cu, Cu-poly, Cu-poly/SiO₂ and Cu-foil, Cu₂O, CuO standard. (g) Morlet wavelet transforms contour plots for the k^3-weighted EXAFS spectra of Cu foil, Cu, Cu-poly and Cu-poly/SiO₂.

standard samples are in alignment with that of Cu foil (Fig. 3c). Further analysis of the locally enlarged XANES spectra show that the absorption edges of Cu in Cu, Cu-poly and Cu-poly/SiO$_2$ are all located between those of Cu foil, Cu$_2$O and CuO reference samples, indicating that the Cu species are in a positive valence between 0 and +2.0 (Fig. 3d). Based on the linear correlation depicted in Fig. 3e, which relates the energy position of standard samples (Cu foil, Cu$_2$O, and CuO) to their oxidation states, the Cu valences in Cu, Cu-poly and Cu-poly/SiO$_2$ are estimated to be +0.64, +0.72, and +1.10, respectively. The higher oxidation of Cu in Cu-poly/SiO$_2$, compared to Cu and Cu-poly can be primarily attributed to oxygenated interface of SiO$_2$.[36]

The Fourier-transformed extended X-ray absorption fine structure (FT-EXAFS) spectra consistently reveal the Cu–Cu and Cu–O scattering paths for Cu, Cu-poly, and Cu-poly/SiO$_2$, exhibiting patterns analogous to those observed in Cu foil (Fig. 3f). Notably, the intensity of the Cu–Cu shell in Cu-poly is higher than that observed in Cu, indicating an increase in the coordination number (CN) of the Cu atom after polymerization. After introducing SiO$_2$, whose surface promotes the enrichment of oxidized species, the signal intensity of the Cu–O shell layer in Cu-poly/SiO$_2$ increases further, closely approaching the level of CuO. These variations in CN and bond length suggest that Cu coordination can be modulated through the incorporation of polymer and SiO$_2$. The scattering paths of Cu–O in Cu exhibit the same trend as those in Cu$_2$O, indicating that the Cu–O bond length in Cu is consistent with that in Cu$_2$O. However, the bond length in Cu-poly and Cu-poly/SiO$_2$ is notably increased, approaching that of the CuO reference, pointing to a more

pronounced oxidation state, resulting from polymerization and the addition of SiO$_2$. In addition to the FT-EXAFS analysis, we also employed the Morlet Wavelet Transform (WT) to simultaneously examine the information in both R-space and k-space. As shown in Fig. 3g, the WT-EXAFS contour map for Cu foil, Cu, Cu-poly, and Cu-poly/SiO$_2$ clearly differentiate peaks corresponding to Cu–O and Cu–Cu bonds in R-space. The peak position of the Cu–Cu bond in Cu and Cu-poly are lower than that in Cu foil, indicating the involvement of O atoms in coordination, leading to a shift in k-space to lower values. Notably, the peak position in k-space for Cu is even lower than those of Cu-poly composites, while the Cu–Cu peak in Cu-poly/SiO$_2$ appears at a higher k-space position than Cu foils, Cu and Cu-poly. This difference implies that, in addition to oxygen, heavier silicon atoms also coordinate with Cu.[33]

Apart from the information about the physical and chemical structures of catalysts, we also evaluated the electrocatalytic performances on Cu and Cu-poly/SiO$_2$ electrodes with the different reaction microenvironments using an MEA cell, benefiting from the characteristics of the zero-gap construction, freedom from catholyte and CO$_2$ direct electroreduction.[37] Fig. S11 and S12, ESI† illustrate the schematic design of the MEA device, along with a depiction of its operational conditions, including the detailed parameters for the GDL, AEM, electrolyte and anode. Cyclic voltammetry (CV) analysis reveals that the current density of HER on the exposed Cu (−10.85 mA cm^{-2}) is obviously higher than that of Cu-poly/SiO$_2$ (−2.67 mA cm^{-2}) under the same applied voltage of 2.0 V (Fig. 4a). This suggests that the dual-hydrophobic Cu-poly/SiO$_2$ effectively
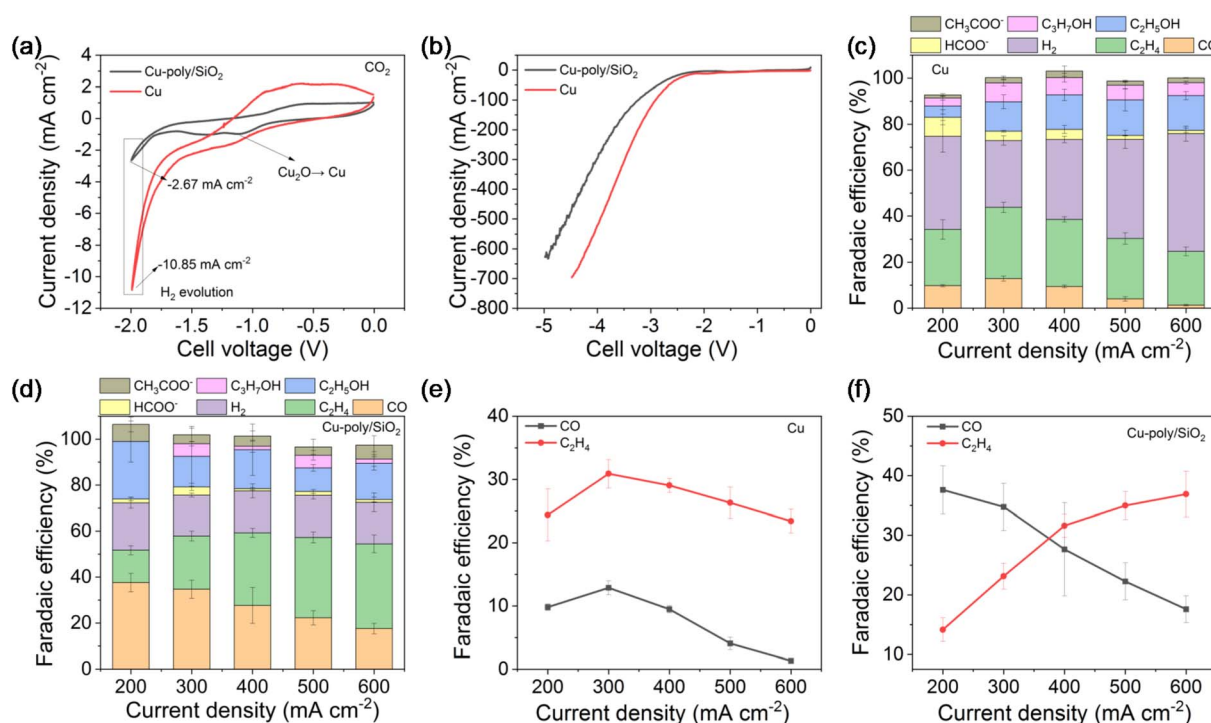

Fig. 4 Electrocatalytic performance of Cu and Cu-poly/SiO$_2$. (a) CV and (b) LSV curves of Cu and Cu-poly/SiO$_2$ in 1 M KHCO$_3$. (c and d) Faradaic efficiency (FE) for (c) Cu and (d) Cu-poly/SiO$_2$. (e and f) FE of CO and C$_2$H$_4$ on (e) Cu and (f) Cu-poly/SiO$_2$ at various current densities.

stops H_2O from reaching the surface of Cu-poly. Corresponding results obtained in an argon atmosphere for Cu, Cu-poly/SiO_2, Cu-poly, and Cu/SiO_2 further support that polymer modification and SiO_2 could suppress the rate of HER (Fig. S13, ESI†). On the one hand, hydrophobic SiO_2 repels H_2O from the bulk electrolyte, preventing it from contacting the catalyst surface, thereby reducing the coverage of H_2O. On the other hand, the polymer also repels H_2O through the organic silane functional groups in its structure, further lowering the H_2O content on the surface of Cu-poly/SiO_2. However, introducing SiO_2 and polymer inevitably leads to partial coverage of the active sites, which consequently diminishes the reduction current of CO_2RR (Fig. 4b and S14, ESI†). These findings indicate the dual-hydrophobic microenvironments of Cu-poly/SiO_2 reduces the local concentration of H_2O, restricting its interaction with catalytic sites, which in turn reduces the hydrogen production rate. A similar trend is also observed on Cu and Cu-poly/SiO_2 when using traditional H-type electrolytic cells (Fig. S15 and S16, ESI†). As depicted in comparative linear sweep voltammetry (LSV) curves of Cu and Cu-poly/SiO_2, an obvious decrease in total current density of CO_2RR is observed on Cu-poly/SiO_2 in contrast to bare Cu at the same cell potentials (Fig. 4b). This reduction is attributed to a decrease in electrochemically active surface area (Fig. S17, ESI†).

To determine the composition of gaseous products, an online gas chromatograph (GC) equipped with a thermal conductivity detector (TCD) and flame ionization detector (FID) was employed. The composition of gaseous products was studied on the different electrodes every 11 min under chronopotentiometry with the current density ranging from 200 to 600 mA cm^{-2}. The primary gas products are H_2, CO, and C_2H_4, over the four main catalysts. The faradaic efficiency (FE) of H_2 over Cu increases from 40.56% at 200 mA cm^{-2} to 51.18% at 600 mA cm^{-2}, while the FE of C_{2+} products rises from 34.08% to 46.11%, accompanied by a partial current density of C_2H_4 from 48.78 to 140.52 at the same current density. Notably, the FE of CO exhibits a lesser extent of variation, fluctuating between 4.07% and 12.88% from 300 to 600 mA cm^{-2}. Unfortunately, the total FEs of products for both Cu and Cu-poly/SiO_2 fluctuate around 100%, due to variations in the volume of the liquid electrolyte during collection procedures (Fig. 4c). For Cu-poly and Cu/SiO_2, the FE of H_2 remains relatively stable at lower current densities but increases at high current densities (Fig. S18, ESI†), due to the individual polymer or SiO_2 incompletely limiting the accessibility of H_2O and enhancing the local concentration of CO_2. In comparison, the FE of H_2 over Cu-poly/SiO_2 ranges from 17.74% at 300 to 20.50% at 200 mA cm^{-2}, while the FE of C_{2+} products of Cu-poly/SiO_2 increases from 46.64% at 200 to 60.54% at 600 mA cm^{-2}, with a partial current density of C_2H_4 ranging from 28.28 to 221.46 mA cm^{-2}, exceeding those of Cu and moderately hydrophobic Cu-poly and Cu/SiO_2 electrodes (Fig. 4d and S18, ESI†). It should be noted that the FE of CO on Cu-poly/SiO_2 fluctuates from 17.57% at 600 mA cm^{-2} to 37.61% at 200 mA cm^{-2}, exceeding that of Cu.

It is worth noting that the FE of C_2H_4 and CO on Cu exhibits a similar trend, with both reaching a peak at 300 mA cm^{-2}. However, the FE of C_2H_4 and CO on Cu-poly/SiO_2 are inversely

proportional, and the FE of C_2H_4 reaches its maximum at 600 mA cm^{-2} (Fig. 4e and f), while CO production is significantly reduced. This observation suggests that the enhanced FE of C_2H_4 on Cu-poly/SiO_2 could be correlated with *in situ* CO, which is more pronounced than that on Cu, Cu-poly and Cu/SiO_2, and plays a critical role in increasing the local CO coverage, thus facilitating the co-electrolysis of CO_2 and generating CO.[38] Moreover, the polymer and SiO_2 appear to reduce the surface H_2O content, thereby limiting the protonation of CO and improving the selectivity of CO product. Similarly, the findings are observed on carbon-paper-supported Cu and Cu-poly/SiO_2 electrodes (Fig. S19, ESI†), with results from the H-type cells aligning with those from the MEA devices (Fig. S20, ESI†). These electrochemical results indicate that a strong correlation between the generation of C_2H_4 and CO, suggesting that modulation of the reaction pathway can be achieved by regulating the catalytic microenvironments.

To gain deep insights into the reaction mechanism, *in situ* attenuated total reflection surface-enhanced infrared absorption spectroscopy (ATR-SEIRAS) was employed to monitor the adsorption behavior, coverage, and bonding information of molecules, ions, and intermediates on Cu and Cu-poly/SiO_2 during CO_2RR.[39] A schematic illustration and digital images of the ATR electrolytic cell are presented in Fig. S21, ESI.† Real-time FTIR spectra were recorded during the CO_2RR over Cu and Cu-poly/SiO_2 within the potential range from the open circuit potential (OCP) to −2.2 V (V *vs.* Ag/AgCl, throughout unless otherwise stated). Two distinct broad adsorption bands at wavenumbers of ~1650 cm^{-1} and ~3400 cm^{-1} were observed and assigned to the bending (δ(OH)) and stretching vibration (ν(OH)) of adsorbed H_2O, respectively (Fig. 5 and S22 ESI†).[40] Notably, the larger peak area of the δ(OH) signal observed on Cu relative to Cu-poly/SiO_2 suggests a higher coverage of H_2O and thus more favorable hydrogen evolution (Fig. S23a†).[15]

A small downward peak emerged at 2100 cm^{-1} on Cu with a potential of −1.1 V, which is attributed to the linear adsorbed CO ν(CO$_L$),[41] and this band shifts towards a lower wavenumber of 2080 cm^{-1} due to the Stark effect (Fig. 5a and S24a, ESI†).[42] Similarly, the wavenumber of ν(CO$_L$) on Cu-poly/SiO_2 appears at 2090 cm^{-1} and exhibits higher intensity compared to that of Cu (Fig. 5b and S24b, ESI†). The larger area of ν(CO$_L$) than that of Cu should be noted, indicating that Cu-poly/SiO_2 could enhance the coverage of *CO and achieve the synergistic electroreduction of reactant CO_2 and *in situ*-generated CO (Fig. S23b†).[29] Notably, a distinct band is located at 1240 cm^{-1}, which is ascribed to the vibration of Si–O–Si due to the Si substrates of both Cu and Cu-poly/SiO_2 (Fig. 5).[43–47]

To elucidate the influence of aerophilic SiO_2 and polymer on the diffusion behavior of CO_2 molecules across the surface of Cu, molecular dynamics (MD) simulations were employed to unravel the underlying interactions. The simulation results indicate that the Cu-poly/SiO_2 system could promptly capture and absorb CO_2 molecules from the surrounding bulk phase within 6 ns, as evidenced by the time sequence of representative snapshots (Fig. 6a). The rapid CO_2 uptake can be attributed to the hydrophobic GDL formed by SiO_2 and polymer components. In a similar fashion, CO_2 molecules also exhibit rapid diffusion on Cu-poly (Fig. 6b) within 6 ns. In contrast, the Cu electrode
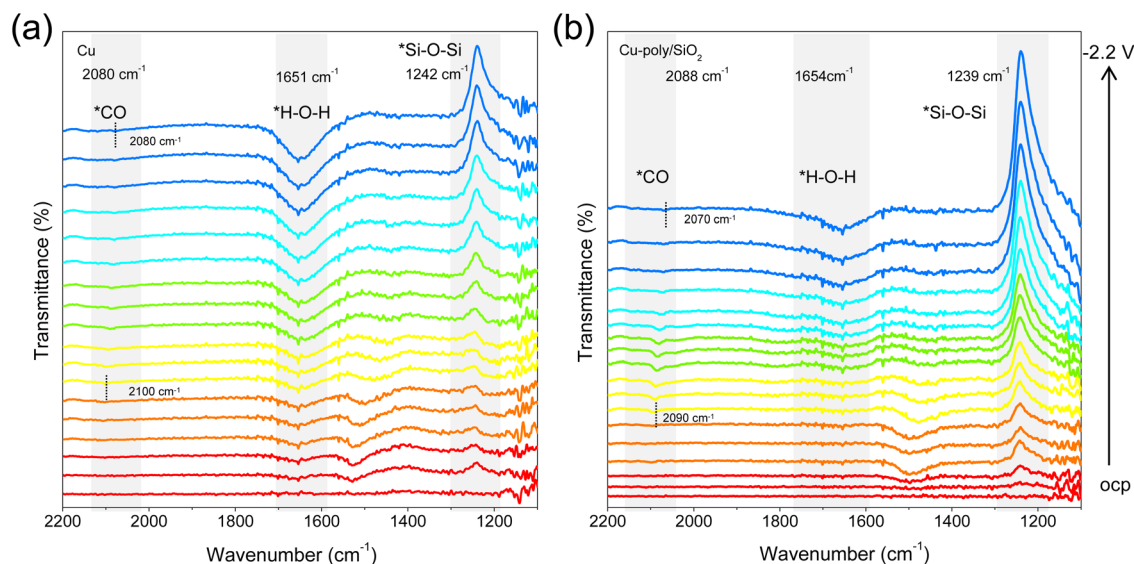
Fig. 5 *In situ* FTIR and synergistic catalytic mechanism. ATR–SEIRAS spectra on (a) Cu NPs and (b) Cu-poly/SiO$_2$ electrode.

repels gaseous CO$_2$, preventing diffusion from the bulk phase (Fig. 6c). Furthermore, the Cu-poly/SiO$_2$ presents more negative system energy (−67.04 eV at 100 ns) compared to the Cu (−0.003 eV at 100 ns), indicating that the dual-hydrophobic catalytic microenvironments present a lower system energy due to the fast CO$_2$ diffusion. Notably, Cu-poly exhibits the lowest system energy (−190.82 eV at 100 ns) compared to the
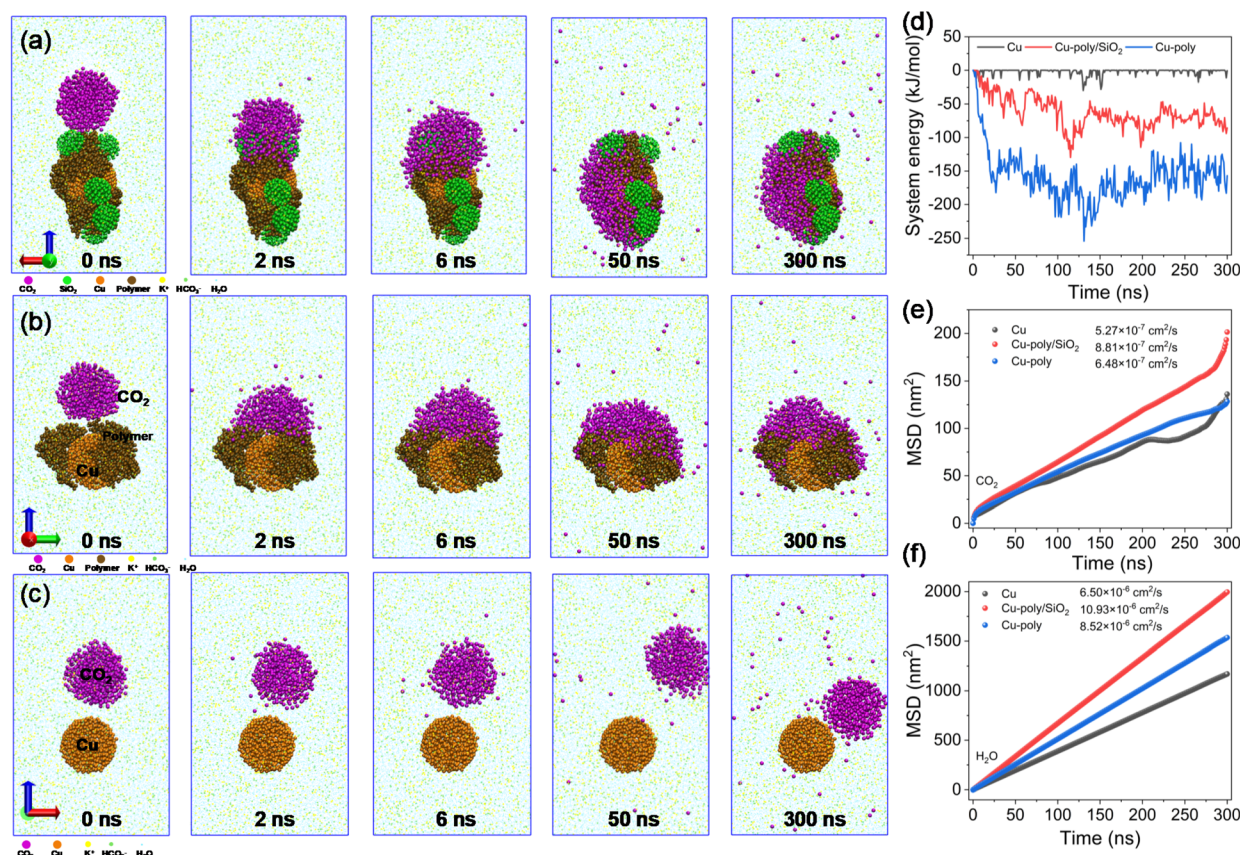

Fig. 6 CO$_2$/H$_2$O diffusion dynamics. Evolution of typical snapshots of CO$_2$ diffusion dynamics on (a) Cu-poly/SiO$_2$ and (b) Cu-poly and (c) Cu NPs. (d) Time-dependent change in system energies of Cu and CO$_2$ molecules on Cu, Cu-poly and Cu-poly/SiO$_2$. (e and f) Mean square displacement (MSD) *versus* time for (d) CO$_2$ and (e) H$_2$O over Cu, Cu-poly and Cu-poly/SiO$_2$. Diffusion coefficients of CO$_2$ and H$_2$O are calculated by the MSD.

other electrodes, indicating that the polymer facilitates stronger adsorption of CO_2 (Fig. 6d).

We further calculated the diffusion coefficients of CO_2 and H_2O over Cu, Cu-poly and Cu-poly/SiO_2 by the mean square displacement (MSD) derived from the MD simulations. These simulations were conducted at a constant temperature of 300 K, with a fixed number of molecules and volume within a duration of 300 ns. The simulation shows that the CO_2 diffusion coefficient increases from 5.27×10^{-7} cm^2 s^{-1} on Cu to 6.48×10^{-7} cm^2 s^{-1} on Cu-poly and reaching 8.81×10^{-7} cm^2 s^{-1} on Cu-poly/SiO_2 (Fig. 6e), demonstrating the fast CO_2 diffusion from the bulk phase to the vicinity of Cu, mainly due to the reduction in diffusion resistance of CO_2 created by the robust hydrophobicity of polymer modification and SiO_2. Correspondingly, the H_2O diffusion coefficient increases from 6.50×10^{-6} cm^2 s^{-1} on Cu to 8.52×10^{-6} cm^2 s^{-1} on Cu-poly and further to 10.93×10^{-6} cm^2 s^{-1} on Cu-poly/SiO_2 (Fig. 6f). This enhancement arises from disruption of the hydrogen-bonding network by nonpolar functional groups ($-CF_3$, $(CH_3O)_3Si-$, and $-CH_3$) in the hydrophobic composite, which promotes the formation of isolated H_2O molecules or small clusters, thereby reducing intermolecular friction. Furthermore, the minimized H_2O-substrate interactions facilitate rapid interfacial water displacement. Consequently, the presence of hydrophobic SiO_2 and polymer largely expedites the diffusion of CO_2 and does not impede the accessibility of H_2O from the bulk electrolyte to the surface of Cu, resulting in simultaneous improvement of the CO_2RR.

Conclusions

In conclusion, we propose a useful strategy for regulating dual-hydrophobic catalytic microenvironments by incorporating SiO_2 into polymer-functionalized Cu, thereby enriching the local concentration of CO_2 and in situ-generated CO product. The optimized Cu-poly/SiO_2 electrode displays an improved current density and selectivity of C_2H_4 compared to bare Cu. Combined in situ ATR-SEIRAS, XAS and MD simulations demonstrate that these enhanced performances can be ascribed to the systematic electrocatalysis of CO_2 and CO, accelerated CO_2 mass transfer dynamics and elevated oxidation state of Cu species. Compared to Cu, Cu-poly/SiO_2 optimizes the local concentration of CO_2, CO, and H_2O, facilitating the co-feeding modes by enhancing the hydrophobicity of GDEs in MEA devices. This work highlights the importance of interfacial and surficial engineering for constructing dual-hydrophobic catalytic microenvironments for Cu and its derivatives, significantly promoting the formation rate of C_{2+} products.

Data availability

The data supporting this article have been included as part of the ESI.†

Author contributions

T. Z. and F. C. conceived the idea and designed the experiments. Y. X. performed MD simulations. Z. Z., X. W., K. L., J. C., K. L., Y. L., M. Y., Z. Y., L. J. analyzed the experimental data. M. Y. and F. C. supervised the project. All authors participated in discussing the results and preparing the manuscript.

Conflicts of interest

The authors declare that they have no known competing financial interests or personal relationships that could have appeared to influence the work reported in this paper.

Acknowledgements

References

1 H. Xu, D. Rebollar, H. He, L. Chong, Y. Liu, C. Liu, C.-J. Sun, T. Li, J. V. Muntean, R. E. Winans, D.-J. Liu and T. Xu, *Nat. Energy*, 2020, **5**, 623–632.

2 M. Fan, J. E. Huang, R. K. Miao, Y. Mao, P. Ou, F. Li, X.-Y. Li, Y. Cao, Z. Zhang, J. Zhang, Y. Yan, A. Ozden, W. Ni, Y. Wang, Y. Zhao, Z. Chen, B. Khatir, C. P. O'Brien, Y. Xu, Y. C. Xiao, G. I. N. Waterhouse, K. Golovin, Z. Wang, E. H. Sargent and D. Sinton, *Nat. Catal.*, 2023, **6**, 763–772.

3 G. Wang, J. Chen, Y. Ding, P. Cai, L. Yi, Y. Li, C. Tu, Y. Hou, Z. Wen and L. Dai, *Chem. Soc. Rev.*, 2021, **50**, 4993–5061.

4 X. Wu, S. Zhang, S. Ning, C. Yang, L. Li, L. Tang, J. Wang, R. Liu, X. Yin, Y. Zhu, S. Chen and J. Ye, *Chem. Sci.*, 2025, **16**, 4568–4594.

5 Y. Wang, J. Liu and G. Zheng, *Adv. Mater.*, 2021, **18**, 2005798.

6 N. Zhang and Y. Zhang, *J. Mater. Chem. A*, 2025, **13**, 2902–2910.

7 M. Zhuansun, Y. Liu, R. Lu, F. Zeng, Z. Xu, Y. Wang, Y. Yang, Z. Wang, G. Zheng and Y. Wang, *Angew. Chem., Int. Ed.*, 2023, **62**, e202309875.

8 Z. Wei, W. Wang, T. Shao, S. Yang, C. Liu, D. Si, R. Cong and M. Cao, *Angew. Chem., Int. Ed.*, 2024, **64**, e202417066.

9 K. Yang, R. Kas, W. A. Smith and T. Burdyny, *ACS Energy Lett.*, 2020, **6**, 33–40.

10 C. Chen, H. Jin, P. Wang, X. Sun, M. Jaroniec, Y. Zheng and S.-Z. Qiao, *Chem. Soc. Rev.*, 2024, **53**, 2022–2055.

11 M. S. Xie, B. Y. Xia, Y. Li, Y. Yan, Y. Yang, Q. Sun, S. H. Chan, A. Fisher and X. Wang, *Energy Environ. Sci.*, 2016, **9**, 1687–1695.

12 C. Kim, J. C. Bui, X. Luo, J. K. Cooper, A. Kusoglu, A. Z. Weber and A. T. Bell, *Nat. Energy*, 2021, **6**, 1026–1034.

13 D. Wakerley, S. Lamaison, F. Ozanam, N. Menguy, D. Mercier, P. Marcus, M. Fontecave and V. Mougel, *Nat. Mater.*, 2019, **18**, 1222–1227.

14 X. Tong, P. Zhang, P. Chen, Z. He, X. Kang, Y. Yin, Y. Cheng, M. Zhou, L. Jing, G. Wang, B. Xu, L. Zheng, X. Xing, Z. Wu and B. Han, *Angew. Chem., Int. Ed.*, 2024, **64**, e202413005.

15 T. Deng, S. Jia, C. Chen, J. Jiao, X. Chen, C. Xue, W. Xia, X. Xing, Q. Zhu, H. Wu, M. He and B. Han, *Angew. Chem., Int. Ed.*, 2023, **63**, e202313796.

16 K. Xu, J. Li, F. Liu, X. Chen, T. Zhao and F. Cheng, *Angew. Chem., Int. Ed.*, 2023, **62**, e202311968.

17 D. Wang, J. Mao, C. Zhang, J. Zhang, J. Li, Y. Zhang and Y. Zhu, *eScience*, 2023, **3**, 100119.

18 H. Rabiee, M. Li, P. Yan, Y. Wu, X. Zhang, F. Dorosti, X. Zhang, B. Ma, S. Hu, H. Wang, Z. Zhu and L. Ge, *Adv. Sci.*, 2024, **11**, 2402964.

19 D. H. Nam, O. Shekhah, A. Ozden, C. McCallum, F. Li, X. Wang, Y. Lum, T. Lee, J. Li, J. Wicks, A. Johnston, D. Sinton, M. Eddaoudi and E. H. Sargent, *Adv. Mater.*, 2022, **34**, e2207088.

20 H.-Q. Liang, S. Zhao, X.-M. Hu, M. Ceccato, T. Skrydstrup and K. Daasbjerg, *ACS Catal.*, 2021, **11**, 958–966.

21 Y. Wu, M. N. Idros, D. Feng, W. Huang, T. Burdyny, B. Wang, G. Wang, M. Li and T. E. Rufford, *ACS Appl. Mater. Interfaces*, 2024, **16**, 56967–56974.

22 M. Zhang, M. Lu, M.-Y. Yang, J.-P. Liao, Y.-F. Liu, H.-J. Yan, J.-N. Chang, T.-Y. Yu, S.-L. Li and Y.-Q. Lan, *eScience*, 2023, **3**, 100116.

23 R. B. Kutz, Q. Chen, H. Yang, S. D. Sajjad, Z. Liu and I. R. Masel, *Energy Technol.*, 2017, **5**, 929–936.

24 Y. S. Cho, S. C. Lin, C. C. Wang, Y. T. Yang, Y. R. Ho and J. J. Huang, *Appl. Phys. A*, 2024, **130**, 663.

25 B. Zhang, J. Zhang, M. Hua, Q. Wan, Z. Su, X. Tan, L. Liu, F. Zhang, G. Chen, D. Tan, X. Cheng, B. Han, L. Zheng and G. Mo, *J. Am. Chem. Soc.*, 2020, **142**, 13606–13613.

26 M. Ding and H.-L. Jiang, *CCS Chem.*, 2020, **2**, 2740–2748.

27 Y. Xu, W. Gao, Z. Chen, Z. Yin, Z. Chen, X. Chang, M. Cheng and B. Xu, *ACS Catal.*, 2024, **14**, 10829–10838.

28 M. Wang, Z. Wang, Z. Huang, M. Fang, Y. Zhu and L. Jiang, *ACS Nano*, 2024, **18**, 15303–15311.

29 X. Wei, Z. Yin, K. Lyu, Z. Li, J. Gong, G. Wang, L. Xiao, J. Lu and L. Zhuang, *ACS Catal.*, 2020, **10**, 4103–4111.

30 L. Wan, Q. Zhou, X. Wang, T. E. Wood, L. Wang, P. N. Duchesne, J. Guo, X. Yan, M. Xia, Y. F. Li, A. A. Jelle, U. Ulmer, J. Jia, T. Li, W. Sun and G. A. Ozin, *Nat. Catal.*, 2019, **2**, 889–898.

31 Y. Xu, X. Li, J. Cao, J. Wang, G. Ma, X. Wen, Y. Yang, Y. Li and M. Ding, *Science*, 2021, **371**, 610–613.

32 T. Zhao, X. Zong, J. Liu, J. Chen, K. Xu, X. Wang, X. Chen, W. Yang, F. Liu, M. Yu and F. Cheng, *Appl. Catal., B*, 2024, **340**, 123281.

33 W.-F. Xiong, D.-H. Si, H.-F. Li, X. Song, T. Wang, Y.-B. Huang, T.-F. Liu, T. Zhang and R. Cao, *J. Am. Chem. Soc.*, 2023, **146**, 289–297.

34 B. Deng, M. Huang, K. Li, X. Zhao, Q. Geng, S. Chen, H. Xie, X. Dong, H. Wang and F. Dong, *Angew. Chem., Int. Ed.*, 2021, **61**, e202114080.

35 X. Yuan, S. Chen, D. Cheng, L. Li, W. Zhu, D. Zhong, Z. J. Zhao, J. Li, T. Wang and J. Gong, *Angew. Chem., Int. Ed.*, 2021, **60**, 15344–15347.

36 T. Zhao, A. Kumar, X. Xiong, M. Ma, Y. Wang, Y. Zhang, S. Agnoli, G. Zhang and X. Sun, *ACS Appl. Mater. Interfaces*, 2020, **12**, 25832–25842.

37 B. Ó. Joensen, J. A. Zamora Zeledón, L. Trotochaud, A. Sartori, M. Mirolo, A. B. Moss, S. Garg, I. Chorkendorff, J. Drnec, B. Seger and Q. Xu, *Joule*, 2024, **8**, 1–18.

38 C. Wei, Y. Yang, H. Ma, G. Sun, X. Wang, Y. Cheng, C. Zhang, B. Yeo, C. He and A. Wong, *Adv. Funct. Mater.*, 2023, **33**, 2214992.

39 H. Li, K. Jiang, S.-Z. Zou and W.-B. Cai, *Chin. J. Catal.*, 2022, **43**, 2772–2791.

40 H. Wang and H. D. Abruña, *J. Am. Chem. Soc.*, 2023, **145**, 18439–18446.

41 Z. Li, Y. Yang, Z. Yin, X. Wei, H. Peng, K. Lyu, F. Wei, L. Xiao, G. Wang, H. D. Abruña, J. Lu and L. Zhuang, *ACS Catal.*, 2021, **11**, 2473–2482.

42 K. Jiang, X.-Y. Ma, S. Back, J. Zhao, F. Jiang, X. Qin, J. Zhang and W.-B. Cai, *CCS Chem.*, 2021, **3**, 241–251.

43 V. T. T. Phan, Q. P. Nguyen, B. Wang and I. J. Burgess, *J. Am. Chem. Soc.*, 2024, **146**, 4830–4841.

44 K. Jiang, K. Xu, S. Zou and W.-B. Cai, *J. Am. Chem. Soc.*, 2014, **136**, 4861–4864.

45 R.-L. Wei, Y. Liu, Z. Chen, W.-S. Jia, Y.-Y. Yang and W.-B. Cai, *J. Electroanal. Chem.*, 2021, **896**, 115254.

46 L. Wang, S.-F. Hung, S. Zhao, Y. Wang, S. Bi, S. Li, J.-J. Ma, C. Zhang, Y. Zhang, L. Li, T.-Y. Chen, H.-Y. Chen, F. Hu, Y. Wu and S. Peng, *Nat. Commun.*, 2025, **16**, 3502.

47 D. Enders, T. Nagao, A. Pucci, T. Nakayama and M. Aono, *Phys. Chem. Chem. Phys.*, 2011, **13**, 4935–4941.